


Dynamically generated patterns in dense suspensions of active filamentsK. R. Prathyusha,¹ Silke Henkes,² and Rastko Sknepnek^{1,3,*}¹*School of Science and Engineering, University of Dundee, Dundee DD1 4HN, United Kingdom*²*Institute of Complex Systems and Mathematical Biology, Department of Physics, University of Aberdeen, Aberdeen AB24 3UE, United Kingdom*³*School of Life Sciences, University of Dundee, Dundee DD1 5EH, United Kingdom* (Received 11 August 2016; revised manuscript received 20 November 2017; published 12 February 2018)

We use Langevin dynamics simulations to study dynamical behavior of a dense planar layer of active semiflexible filaments. Using the strength of active force and the thermal persistence length as parameters, we map a detailed phase diagram and identify several nonequilibrium phases in this system. In addition to a slowly flowing melt phase, we observe that, for sufficiently high activity, collective flow accompanied by signatures of local polar and nematic order appears in the system. This state is also characterized by strong density fluctuations. Furthermore, we identify an activity-driven crossover from this state of coherently flowing bundles of filaments to a phase with no global flow, formed by individual filaments coiled into rotating spirals. This suggests a mechanism where the system responds to activity by changing the shape of active agents, an effect with no analog in systems of active particles without internal degrees of freedom.

DOI: [10.1103/PhysRevE.97.022606](https://doi.org/10.1103/PhysRevE.97.022606)**I. INTRODUCTION**

Processes that involve active motion and remodeling of protein filaments are particularly important for the functioning of a cell [1]. In particular, the dynamics of cytoskeletal actin filaments are characterized by a constant supply of mechanical energy by myosin motor proteins, which hydrolyze ATP to slide along actin filaments [2,3]. This directed motion is integral to cell migration [4,5]. Motility assays [6,7] have served as simple yet elegant model systems for *in vitro* studies of many active cellular processes. In motility assays, filaments are driven by molecular motors that are typically grafted to a flat substrate, with the energy required for their active motion supplied by ATP. The basic design of motility assays enables a reasonably accurate control of the key parameters, which would be very hard to achieve *in vivo*. Despite their simplicity compared to actual cells, actively driven *in vitro* filaments exhibit fascinating self-organized motion patterns [8–12]. Understanding and characterizing these patterns has been a focus of active research [13–16].

Only several studies to date have investigated the collective motion and pattern formation in the high density regime. For example, Sumino *et al.* [17] reported the existence of an intriguing vortex state in a motility assay of microtubules driven by dynein motor proteins. Large vortices with an average diameter exceeding the mean length of individual filaments by more than an order of magnitude form a lattice structure on sufficiently long time scales. Furthermore, working with actin filaments propelled by heavy meromyosin motors attached to a coverslip, Schaller *et al.* [18] identified several interesting collective motion patterns as a function of the actin density.

Interesting collective behavior of actively driven filamentous systems is not restricted to motility assays [19]. Equally fascinating motion patterns arise in low-density mixtures of microtubules suspended at the oil-water interface and propelled by ATP driven kinesin motors [20–22], where flow is accompanied by spontaneous generation [20] of motile topological defects (so-called active turbulence [23,24]) and the development of orientational order of those defects [22]. Many of the qualitative features observed in these experiments have been reproduced using continuum models for active nematics [23–26]. Finally, in an experiment by Keber *et al.* [21], the microtubule-kinesin mixture was suspended onto the surface of a nearly spherical lipid vesicle. The presence of nonzero curvature leads to an even richer set of collective motion patterns that are only partly understood [27,28].

Finally, bacterial colonies provide another example of elongated active agents with rich collective behavior. Myxobacteria, for example, form a striking variety of collective motion patterns [29] without any long-range chemical signals, but solely due to short-range steric effect and rodlike cell shape [30].

Many of the nonequilibrium patterns observed in motility assays, such as asters and vortices, can be described by the active gel theory [13,31–33]. Continuum description of the active gel theory have been augmented by studies of a number of numerical models with different levels of microscopic details [34–39]. Many of those models are, however, rather simplified and assume stiff, rodlike filaments and/or ignore steric effects. In addition, the effects of hydrodynamics interactions mediated by the flow of the fluid surrounding filaments are also often omitted.

In the dilute regime, steric interactions play a limited role and insights can be gained by studying individual filaments [40–44] or hydrodynamic equations derived from microscopic models [45–47]. Studies of individual active filaments either

*r.sknepnek@dundee.ac.uk

pivoting or freely swimming showed that activity can drive conformational transformations [48], such as spiralling and spontaneous beating [42,49,50], both in the presence and absence of hydrodynamic interactions. Balancing the bending moment with the torque produced by the active force shows [49,50] that activity increases the tendency of the filament to buckle, thus reducing its persistence length. Similar effects have also been observed in models that treat activity as time-correlated random forces [51–53].

It is important to note that most microscopic derivations of continuum equations assume the dilute limit and only consider binary collisions between filaments. For dense systems, considering only binary collisions is not justifiable and it is no longer possible to relate parameters of the microscopic model to the parameters in the effective continuum theory. Numerical simulations are, therefore, crucial to understanding the collective behavior of dense active systems.

In this paper, we explore the collective motion patterns of a dense planar layer of active semiflexible filaments. We use Langevin dynamics simulations to study out of equilibrium behavior of a bead-spring filament model in the presence of steric repulsion. Inspired by the activity mechanism of motility assays, the driving force acts along the contour of the filament. Our model includes frictional coupling to the environment, but ignores the effects of flow. While the importance of hydrodynamic effects in motility assay experiments is still under debate, the experiments of Sumino *et al.* [17] suggest that omitting long-range hydrodynamic interactions in these systems is justifiable. This also significantly reduces the high computational cost associated with simulating significant system sizes with this model.

We map a nonequilibrium phase diagram as a function of activity and stiffness of filaments and identify five distinct phases. A polymer melt phase is followed by a flowing melt region with signatures of both polar and nematic symmetries as activity increases. For stiffer filaments, further increase in activity leads to a phase segregated state akin to the motility induced phase segregation observed for isotropic active particles [54] (MIPS). For flexible filaments, increase in activity leads to a swirling state. Finally, for high activities we observe a rotating spiral phase where filaments adjust their conformation to accommodate the activity. This is contrary to the behavior observed in models of structureless active particles where MIPS becomes more prominent with increasing activity [55].

The paper is organized as follows. In Sec. II we discuss a coarse-grained model for semiflexible filaments subject to an active force acting along the contour of each filament. In Sec. III we present and discuss results of detailed Langevin dynamics simulations and map the nonequilibrium phase diagram. Finally, in Sec. IV we summarize our main findings, comment on potential experimental realizations, and discuss how the model could be extended to describe specific experiments. In Appendix A we compare Langevin dynamics simulations with the more commonly used Brownian dynamics studies.

II. MODEL

We adapt the model recently used by Isele-Holder *et al.* [42] to study conformations of a single semiflexible filament under the influence of an active force of constant magnitude

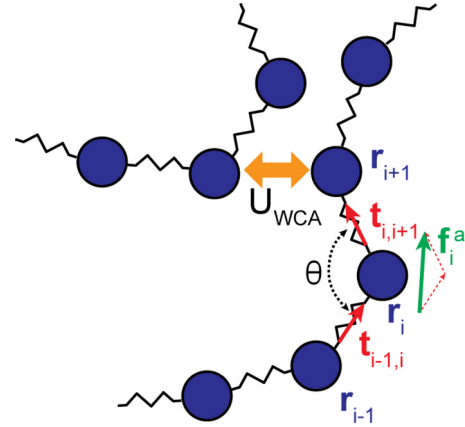


FIG. 1. Schematic representation of the model for self-propelled semiflexible filaments. Spherical beads of diameter σ are connected through harmonic springs of spring constant k_b . The filament flexibility is modeled as a bending penalty for angle θ with stiffness constant κ . Beads belonging to different chains, as well as beads on the same chain that are more than two beads apart, interact via a short-range, repulsive interaction, modeled with the Weeks-Chandler-Andersen potential. Finally, each bead is subject to an active force \mathbf{f}_i^a pointing along the tangent to the filament contour at i . Note that, for clarity, distances between beads along the filament have been exaggerated.

acting along its contour (Fig. 1). Our system consists of M such filaments confined to a periodic square region of length L_{box} . Each filament is modeled as a chain of N beads of diameter σ , so that all filaments have the same degree of polymerization. In most simulations, the packing fraction $\phi = (MN\sigma^2\pi)/4L_{\text{box}}^2$ was set to $\phi \approx 0.65$. This particular choice of the packing fraction ensures that the system is dense on one hand, but, on the other hand, it remains below both the packing fraction of the triangular lattice and random close packing. In other words, there is nothing special about $\phi \approx 0.65$, except that it is high enough that steric effects cannot be ignored but also low enough for the system to be sufficiently far away from being jammed.

Interactions between beads are modeled with bonded and short-range nonbonded pair potentials, i.e., $U = U_B + U_{NB}$. Bonded interactions, $U_B = U_s + U_b$, account for both chain stretching, modeled with the FENE bond potential [56],

$$U_s(r_{ij}) = -1/2k_b R_0^2 \ln(1 - (r_{ij}/R_0)^2), \quad (1)$$

and bending, modeled with the standard harmonic angle potential [57],

$$U_b = \kappa(\theta - \pi)^2. \quad (2)$$

Here, κ is the bending stiffness, θ is the angle between three consecutive beads, $R_0 = 1.3\sigma$ is the maximum bond length, $k_b = 3300k_B T/\sigma^2$ is the bond stiffness (making the chain effectively nonstretchable), and $r_{ij} \equiv |\mathbf{r}_{ij}| = |\mathbf{r}_i - \mathbf{r}_j|$ is the distance between beads at positions \mathbf{r}_i and \mathbf{r}_j . For a stiff filament, the bending stiffness κ in the discrete model is related to the continuum bending stiffness, $\tilde{\kappa}$, as $\kappa \approx \tilde{\kappa}/2b$, where b is the average bond length. Nonbonded interactions, U_{NB} , account for steric repulsions and are modeled with the

Weeks-Chandler-Anderson potential [58],

$$U_{WCA}(r_{ij}) = 4\varepsilon \left[\left(\frac{\sigma}{r_{ij}} \right)^{12} - \left(\frac{\sigma}{r_{ij}} \right)^6 + \frac{1}{4} \right], \quad (3)$$

where ε measures the strength of steric repulsion. These parameters lead to $b \approx 0.86\sigma$, which ensures that filaments do not intersect. Finally, $L = (N - 1)b$ is the mean filament length and T is set to $0.1\varepsilon/k_B$ in all simulations.

The active force on bead i is modeled as

$$\mathbf{f}_i^a = f_p(\mathbf{t}_{i-1,i} + \mathbf{t}_{i,i+1}), \quad (4)$$

which mimics active driving produced by a homogeneous distribution of molecular motors on the substrate underneath the filaments. Here, f_p is the strength of the force and $\mathbf{t}_{i,i+1} = \mathbf{r}_{i,i+1}/r_{i,i+1}$ is the unit-length tangent vector along the bond connecting beads i and $i + 1$; end beads have only contributions from one neighboring bond. We note that the active force in Eq. (4) is slightly different than the active force used in Ref. [42], where the tangent vectors \mathbf{t}_{ij} were not normalized. Given that filaments are effectively unstretchable, the difference between the two expressions for active force is just a scaling factor of order one. We point out that an important, but unsolved question is how important the precise microscopic driving mechanism is for long-range collective behavior. Here we simply note that the extensible nematic system, such as in the experiments of Sancez *et al.* [20], is driven by pair forcing of filaments opposite to each other [47]. Unidirectional forcing, as implemented here, has been shown by two of us to lead to a mix of polar and nematic properties [28], a result that we recover here.

In experiments, filaments are surrounded by a fluid that mediates long-range hydrodynamic interactions. Here we consider the dry limit, where the damping from the medium dominates over hydrodynamic interactions and the surrounding fluid only provides single-particle friction. In this regime, the filament dynamics is described by Langevin equations of motion:

$$m_i \ddot{\mathbf{r}}_i = \mathbf{f}_i^a - \gamma \dot{\mathbf{r}}_i - \nabla_{\mathbf{r}_i} U(r_{ij}) + \mathbf{R}_i(t), \quad (5)$$

where $m_i = 1$ is the mass of bead i . Time is measured in units of $\tau = \sqrt{m\sigma^2/\varepsilon}$. $\mathbf{R}_i(t)$ is a delta-correlated random force with zero mean and, as required by the fluctuation-dissipation theorem, variance $\langle \mathbf{R}_i(t) \cdot \mathbf{R}_j(t') \rangle = \langle R_i^x(t) R_j^x(t') \rangle + \langle R_i^y(t) R_j^y(t') \rangle = 4\gamma k_B T \delta_{ij} \delta(t - t')$, where γ is the friction coefficient, and the prefactor 4 reflects the fact that the system is confined to two dimensions. Equations (5) were integrated with time step $\Delta t = 10^{-3}\tau$ using LAMMPS [59], with an in-house modification to include the active propulsion force. A typical configuration contained $\approx 5 \times 10^4$ beads and was generated by placing chains at random into the simulation box ($L_{\text{box}} = 250\sigma$), making sure that there were no intersections. This configuration was then relaxed for $10^4\tau$, followed by a production run of $10^5\tau$.

We briefly comment on the use of Langevin dynamics. Mesoscopic active systems are typically at very low Reynolds numbers and inertial effects are negligible. Therefore, most models from the outset assume the overdamped limit and use first order equations of motion, where the mass term is omitted. However, there is no *a priori* reason that prohibits

the inertial term from being retained. In dense systems with steep short-range repulsive interactions, retaining it turns out to be computationally beneficial as it allows the use of a significantly larger simulation time step [60] compared to what is possible with the Brownian dynamics approach. We exploit the fact that there is a separation of time scales between individual bead collisions and the mesoscopic dynamics. As we show in Appendix A, the behavior of the system at the time scales associated with collective flow is identical regardless of whether Langevin or Brownian dynamics is used.

Our key parameters are the degree of polymerization, $N \in \{5, 10, 25, 50\}$, the filament stiffness, $\kappa = 1 - 20k_B T$, and the magnitude of the active force, $f_p = 2 \times 10^{-4} - 1k_B T/\sigma$. We identify two dimensionless numbers: the relative filament stiffness or scaled persistence length,

$$\frac{\xi_p}{L} = \frac{\tilde{\kappa}}{Lk_B T} = \frac{2b\kappa}{Lk_B T}, \quad (6)$$

where $\xi_p = 2b\kappa/k_B T$ is the thermal (i.e., passive) persistence length, and the active Péclet number,

$$\text{Pe} = \frac{f_p L^2}{\sigma k_B T}. \quad (7)$$

As previously shown [48,50], the flexure number, $\tilde{\mathfrak{F}} = f_p L^3/\kappa = \sigma^2 \text{Pe}/(\xi_p/L)$, controls the buckling instabilities of a single active filament. Meanwhile, the Péclet number controls the onset of the MIPS state in systems of isotropic active Brownian particles [55].

III. RESULTS AND DISCUSSION

We start by constructing a detailed nonequilibrium phase diagram for this system and proceed to describe and characterize several different motion patterns. While there are similarities with the behavior of a single active filament [42], the combination of self-avoidance and flexibility in dense suspensions leads to interesting collective behavior even in the absence of any explicit aligning interactions. In Fig. 2 we show the phase diagram in the ξ_p/L vs Pe plane with snapshots of the simulations in the four main nonequilibrium phases shown in Fig. 3 (see also movies in the Supplemental Material [61]). It is also important to note that the phase behavior of the system can be fully described by the two dimensionless numbers, Pe and ξ_p/L .

In order to characterize the nature of the flow in the system we computed the mean squared displacement (MSD) of the center of mass of filaments, averaged over all filaments [Fig. 4(a)]. Without activity (i.e., for Pe = 0), after the usual short time ballistic relaxation, the MSD curve shows subtly subdiffusive dynamics with exponent ≈ 0.8 indicating slow dynamics resembling supercooled liquids. As expected, activity introduces flow, leading to the melt phase. For low activity, steric effects dominate and the system resembles a conventional polymer melt where activity acts only as a weak perturbation. It is interesting to note that for flexible filaments ($\xi_p/L \lesssim 0.1$) at Pe $\gtrsim 1$ the diffusion coefficient increases linearly with Péclet number [inset, Fig. 4(b)]. While it is not surprising that the diffusion coefficient increases with activity (see also Ref. [53]), the origin of the linear dependence on the Pe is at present not clear.

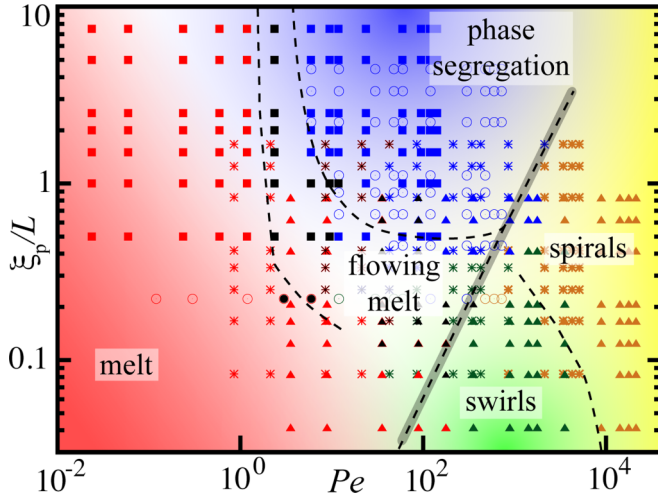


FIG. 2. Nonequilibrium phase diagram for ξ_p/L vs Pe at packing fraction $\phi = 0.64905$. Results for different filament lengths are plotted on the same graph since they show the same scaling. Symbols mark individual simulations for different filament lengths: $N = 5$ (■), $N = 10$ (○), $N = 25$ (*), and $N = 50$ (▲), with phases coded by color. Different phases were identified by visually inspecting each individual run. Crossovers between phases are indicated by shading. Dashed lines indicate rough boundaries between phases and serve as a guide to the eye. The gray-shaded bar indicates the threshold to spiraling, set by the flexure number $\xi \approx 10^3$ [42].

Stiffer filaments, on the other hand, exhibit a transition from subdiffusive to superdiffusive flow at $Pe \approx 1$. For longer filaments, in this flowing melt regime, one observes $\pm 1/2$ topological defects [Fig. 3(a)] reminiscent of those seen in the experiments of Sanchez *et al.* [20]. However, it is important to note that there are two important differences between the structure of the defects observed in our simulations and those seen in the experiments of Sanchez *et al.* First, experiments are performed at much lower densities than studied here and, second, in the experiments individual microtubules only slightly bend, nowhere near the fully bent hairpin configuration observed in this study. It is also still not completely clear if long-ranged hydrodynamics interactions have an important effect on the dynamics in the experimental system.

In our simulations, defect motion is very slow and is driven by filaments sliding along their contour. It is straightforward to properly identify and track the defects, e.g., by using a version of the algorithm proposed by Zapotocky *et al.* [28,62], as outlined in Appendix B. However, at the time scales accessible to our simulations, defects move over very short distances, insufficient to extract meaningful information about their dynamics. Therefore, we did not attempt to study the defect dynamics in detail, but instead we applied the defect finding algorithm only to several selected snapshots of the simulation to showcase their existence. We note that defect motion in self-propelled systems appears to generally be much slower than individual particle motion [28,63].

As the filament stiffness increases ($\xi_p/L \gtrsim 0.2$), large bends become costly and at sufficiently high Péclet numbers, $Pe \gtrsim 10$, similar to the Péclet threshold in MIPS of self-propelled particles [55], the system crosses over into a phase-segregated state [Fig. 3(c)] characterized by filaments aligning and flowing as a coherent bundle. The mechanism that leads to this behavior can be explained as follows. When multiple filaments collide with each other in a head-to-front manner, steric interactions align them into bundles that propagate coherently [41]. This, however, happens only if filaments are sufficiently stiff since, for soft filaments, fluctuations in the direction of motion prevent them from bundling (see Supplemental Material [61]). Bundles break up due to collisions with filaments in surrounding bundles and thermal noise. Typically, we observe several large clusters moving in different directions. The cluster size depends on the density of filaments (in the dilute regime this aggregation is absent; see also movies in Supplemental Material [61]). The motion of the bundles is accompanied by substantial density fluctuations [white regions in Fig. 3(c)], akin to those seen in the MIPS phase of self-propelled disks and rods. Once formed, the entire bundle retains its direction over an extended period of time, in some cases comparable to the length of the entire simulation. This can be seen in the MSD curves [Fig. 4(a)], which show wide regions of persistent, $\sim t^2$, behavior. At long times, however, the direction of motion of bundles decoheres and diffusive behavior is recovered. It is interesting that the transition time, τ_c , of the onset of diffusive behavior reduces with activity as $\tau_c \sim (Pe)^{-\zeta}$, with $\zeta \approx 0.9-1.5$, where the exponent ζ increases with filament stiffness (Fig. 5). A similar activity-dependent

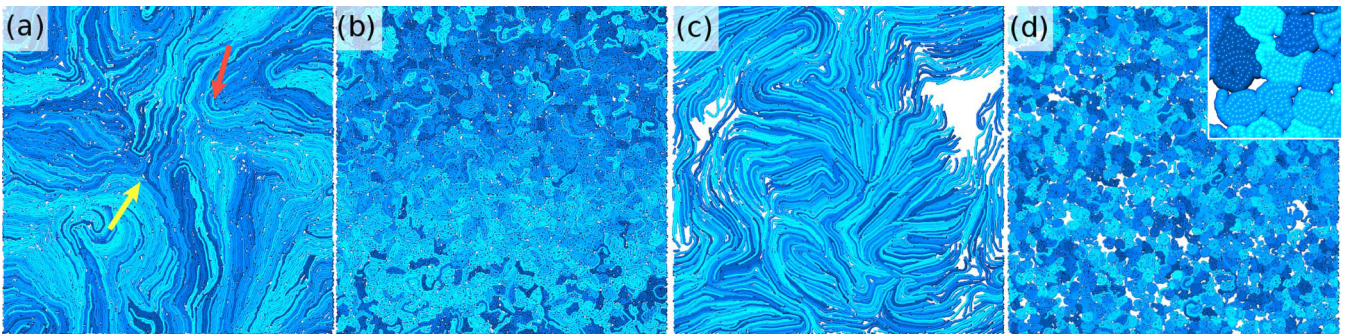


FIG. 3. Snapshots of simulations for $N = 50$ in four nonequilibrium phases: (a) flowing melt ($\xi_p/L = 0.2$, $Pe = 35.5$), (b) swirl ($\xi_p/L = 0.04$, $Pe = 177.58$), (c) segregated phase ($\xi_p/L = 0.82$, $Pe = 355.16$), and (d) spirals ($\xi_p/L = 0.04$, $Pe = 17757.8$). Individual filaments are marked by a different shade. Arrows in (a) point to examples of $+1/2$ (red) and $-1/2$ (yellow) topological defects. White areas in (c) are regions devoid of filaments, indicating substantial density fluctuations. Inset in panel (d) is a zoom-in on several spirals.

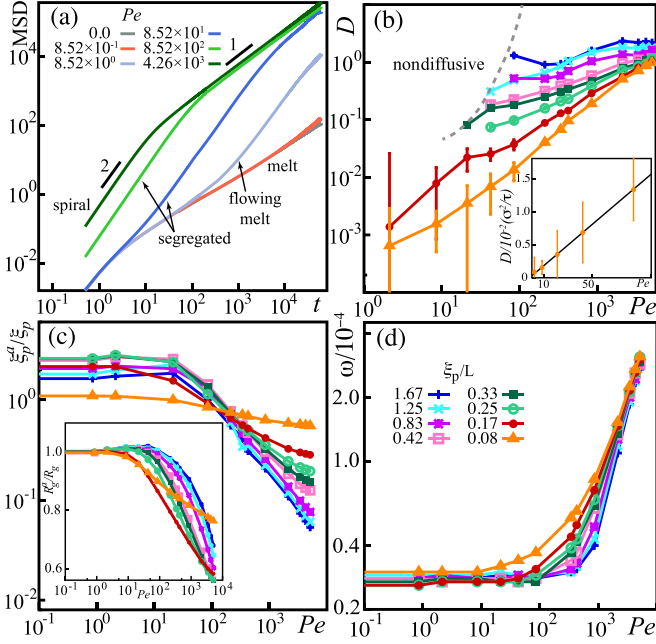


FIG. 4. (a) Mean-square displacement (MSD) as a function of time for $\xi_p/L \approx 0.83$ for six values of $Pe = 0, 0.852, 8.52, 85.2, 852, 4260$. (b) Log-log plot of the diffusion coefficient as a function of Pe in the regime where the system is diffusive. *Inset*: linear scaling at low activity for a soft ($\xi_p/L = 0.08$) filament. (c) Ratio of active (ξ_p^a) to passive ($\xi_p = 2\kappa b/k_B T$) persistence length for a range of values of bare bending stiffnesses. Note that due to steric effects the measured persistence length at low activity is always larger than ξ_p . *Inset*: ratio of active, R_g^a , to passive, R_g , radius of gyration as a function of Pe . (d) Average angular velocity of rotation ω defined in Eq. (9) around centers of mass of filaments as a function of Pe . Legend in (d) also applies to panels (b) and (c). $N = 25$ in all plots.

decrease of τ_c has been observed in single-filament studies [42].

The phase-segregated state is not stable for large Péclet numbers. For $Pe \approx 10^2 - 10^4$ and $\xi_p/L \lesssim 0.2$ the system enters

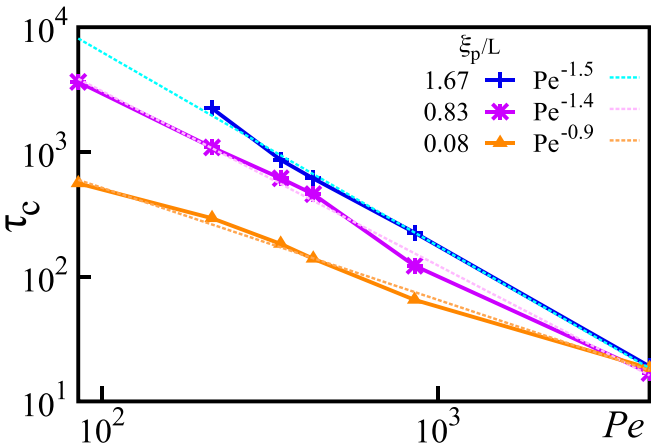


FIG. 5. Transition time from superdiffusive to diffusive behavior in the segregated phase as a function of Péclet number for $\xi_p/L = 0.08, 0.83, \text{ and } 1.67$.

the swirling state [Fig. 3(b)], in which the dynamics is dominated by large fluctuations of filament shapes with individual filaments forming short-lived spirals that quickly uncoil. In this regime, semiflexible filaments are actively pushed against each other enhancing shape fluctuations which prevents formation of large-scale flow patterns.

The onset of the instability is controlled by the flexure number, \mathfrak{F} . We find a similar threshold, $\mathfrak{F} \approx 10^3$, as in the single-filament case [42] (gray-shaded region in Fig. 2). For $Pe \gtrsim 10^3$, the coherently moving bundles dissolve and the system regains a nearly uniform density. The structure of this state is markedly different from the low activity case. Most filaments curl into long-lived spirals [Fig. 3(d)]. While the head bead of the filament is always in the center, there is no preferred direction of the rotation, i.e., there is no global chirality. Centers of spirals move diffusively [Fig. 4(a)]. If the system density is reduced, the state resembles a weakly interacting gas of rotating spirals (see Supplemental Material [61]). It is interesting to ask why the system prefers this unusual spiralling state, as opposed to, e.g., a configuration where perfectly aligned fully stretched filaments flow parallel to each other, which would be preferential energetically. We argue that it is ultimately connected to the conformational entropy of the chains: straight filament configurations are entropically costly and spontaneous shape fluctuations would affect the entire flow. On the other hand, the entropically favorable coiled conformations are not compatible with the self-propulsion which prefers coherent motion with a constant speed $\approx f_p/\gamma$. Therefore, the system balances these two competing effects by selecting filament conformations that trap most activity into circular motion. This mechanism has no analog in systems of simple structureless active agents and owes its existence solely to the extended nature of the filaments, as can also be seen by reducing N , which leads to the disappearance of the spiralling state.

In order to characterize the spiralling state, we compute the average angular velocity of filaments around their centers of mass. The instantaneous angular velocity of filament j is

$$\omega_j(t) = \frac{1}{N} \sum_{i=1}^N \frac{[\mathbf{r}_i(t) - \mathbf{r}_{j,cm}(t)][\mathbf{v}_i(t) - \mathbf{v}_{j,cm}(t)]}{|\mathbf{r}_i(t) - \mathbf{r}_{j,cm}(t)|^2}, \quad (8)$$

where $\mathbf{r}_i(t)$ and $\mathbf{v}_i(t)$ are, respectively, the position and velocity of the bead i at time t . Similarly, $\mathbf{r}_{j,cm}(t)$ and $\mathbf{v}_{j,cm}(t)$ are the instantaneous position and velocity of the center of mass of filament j , respectively. The average magnitude of the angular velocity per filament is then

$$\omega = \frac{1}{M} \sum_{j=1}^M \left| \frac{1}{\tau_m} \sum_t \omega_j(t) \right|, \quad (9)$$

where τ_m is the measurement time. We note that the order in which averages are taken is important to properly capture rotations of individual filaments and also that ω retains a small but finite plateau at low Pe . In Fig. 4(d) we show that ω increases sharply from its plateau value as a function of Péclet number as the buckling threshold is crossed, confirming that individual spirals rotate. The rate of the increase of ω with Pe grows with filament stiffness, which is not surprising as softer filaments are easier to bend.

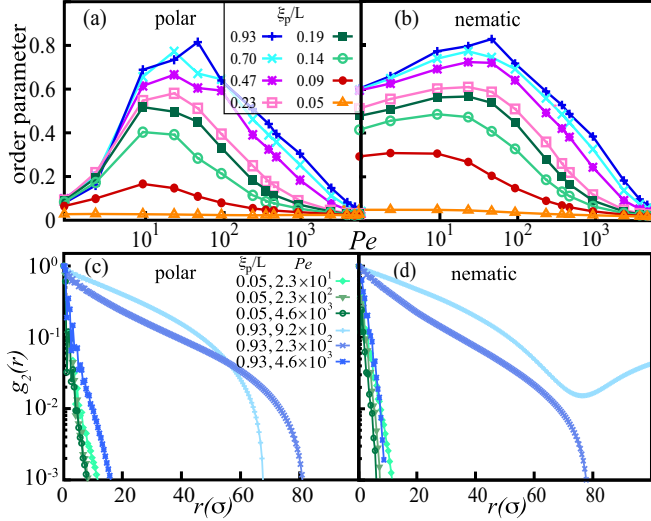


FIG. 6. Local polar (a) and nematic (b) order parameter defined in Eq. (10) as a function of activity for a range of bare filament stiffnesses for $N = 25$. Spatial correlation function $g_{m,2}(r)$ defined in Eq. (11) for the polar (c) and nematic (d) order parameter. Note that the upturn in (d) is an artifact of averaging for large r .

One of the identifying features of self-propelled filaments is the reduction of the effective bending stiffness manifested as the decrease of the effective persistence length, ξ_p^a . The persistence length, ξ_p^a , is determined by fitting the tangent-tangent correlation function $\langle \mathbf{t}(s) \cdot \mathbf{t}(0) \rangle$ to $\exp(-s/\xi_p^a)$, where s measures the position along the contour. In Fig. 4(c) we show the ratio of the persistence length in the presence of activity and its passive, thermal value, ξ_p^a/ξ_p as a function of Pe for a range of bare bending stiffnesses, κ . For low values of Pe , ξ_p^a/ξ_p remains close to 1, indicating that the filament stiffness is not affected by activity. However, as the activity increases, one observes a rapid decrease of the persistence length. This activity-driven reduction of ξ_p^a is accompanied by a drop in the radius of gyration [Fig. 4(c), inset], indicating that the system transitions into a coiled state.

Finally, we explore how orientational order of semiflexible filaments emerges from self-propulsion. Steric repulsion leads to local alignment which does not depend on the filament direction and, therefore, has nematic symmetry. On the other hand, self-propulsion introduces directionality, i.e., filament polarity. Therefore, we compute both polar and nematic local order parameter of the filament tangent vector $\mathbf{t}_i \equiv (\mathbf{r}_i - \mathbf{r}_{i-1})/|\mathbf{r}_i - \mathbf{r}_{i-1}|$; let θ_{ij} be the angle between tangent vectors \mathbf{t}_i and \mathbf{t}_j , belonging to the same or different filaments. Then the order parameter is

$$S_m = \langle \cos(m\theta_{ij}) \rangle, \quad (10)$$

with $m = 1$ for polar, $m = 2$ for nematic, and where the average $\langle \cdot \rangle$ is over all pairs within a cutoff distance, 5σ .

In Fig. 6(a) we show the local polar order parameter S_1 as a function of Pe . For low Pe , the effects of activity are very weak and there is essentially no polar ordering. As the activity increases, filaments align their propulsion directions and start to flow as a bundle, leading to a boost in S_1 for the intermediate values of Pe . At large activities, the system collapses into the

spiralling phase and the order disappears. We observe similar behavior for the local nematic order S_2 [Fig. 6(b)]; however, at low activity the system exhibits substantial local nematic order, consistent with passive polymer melts [64].

In order to probe the extent of the local order in Figs. 6(c) and 6(d) we show the spatial pair correlations of both polar and nematic order parameters of tangent vectors \mathbf{t}_i and \mathbf{t}_j separated by a distance r :

$$g_{m,2}(r) = \frac{\langle \sum_{i,j} \delta(r - |\mathbf{r}_i - \mathbf{r}_j|) \cos(m\theta_{ij}) \rangle}{\langle \sum_{i,j} \delta(r - |\mathbf{r}_i - \mathbf{r}_j|) \rangle}. \quad (11)$$

In all regimes, we observed an exponential decay of $g_{m,2}$. There is, however, a clear difference between flexible and stiff filaments in terms of the extent of spatial correlations. For flexible filaments the order is indeed local and $g_{m,2}$ rapidly drops to zero at distances $\sim 10\sigma$. However, for stiff filaments, both polar and nematic order persist over much longer distances, reaching a fifth of the system size. In the high activity regime, coiling into spirals, however, completely destroys the order even for the stiffest filaments.

IV. SUMMARY AND CONCLUSIONS

In this paper we used Langevin dynamics simulations of an agent-based model to study collective behavior of a dense suspension of semiflexible filaments subject to an active force acting in the direction of the filaments' contours. We took steric effects into account, preventing any intersections between filaments. Furthermore, we assumed the dry limit, i.e., solvent-mediated hydrodynamic interactions were ignored, an assumption that is justifiable when modeling motility assay experiments. We mapped a detailed nonequilibrium phase diagram as a function of activity, measured in terms of the Péclet number Pe , and filament stiffness, measured as the ratio of the passive persistence length to the filament length, ξ_p/L , for several filament lengths.

The intricate interplay between activity and conformational changes leads to rich collective behavior in this system. In particular, at low activity, we found a slowly flowing meltlike state, with prominent half-integer topological defects. Those defects, however, are moving very slowly, consistent with other studies of self-propelled nematics.

At intermediate values of activity we observed phase segregation into a state of aligned bundles akin to a MIPS phase. Finally, at very high activity, this state disappears and we observed a peculiar spiralling state characterized by filaments predominantly curling themselves into rotating spirals. In this state, the density is again uniform with no global flow. This suggests a mechanism by which the system expels activity in part by changing the conformation of the filaments. To the best of our knowledge, this effect has no analog in systems of active agents with no internal structure.

It would be interesting to fully characterize the nature of the flowing melt phase, where one observes spontaneous formation of half-integer topological defects. Preliminary results for a related model where activity acts on pairs of polymers show extensile active dynamics at the time scale of polymer motion and no polar components to the flow, hinting at a fundamental role of the local symmetry of active driving.

The model studied in this paper is too simplified to quantitatively describe a specific experiment. However, it captures several generic collective active patterns and we hope that results presented here will motivate further research in the effects of activity on collective behavior of dense filamentous systems. In particular, experiments on motility assays could provide realizations of some of the phases reported here, especially in the region of phase space where filaments are sufficiently stiff.

Another interesting system for which our results could be of value are experiments on clustering of myxobacteria during the vegetative phase [65]. Myxobacteria are known to form a rich variety of collective patterns despite the absence of any long range interactions, such as chemotaxis [29]. A direct application of our model to swimming bacteria might, however, be affected by long-range hydrodynamic effects. While hydrodynamic effects seem to play a limited role in the collective motion of *E. Coli* [66], the importance of fluid-mediated interaction in, e.g., the longer *B. subtilis* is less clear [67,68] and such effects may play a non-negligible role for the even longer Myxobacteria.

ACKNOWLEDGMENTS

R.S. acknowledges the support from UK EPSRC (Grant No. EP/M009599/1) and S.H. acknowledges support from UK BBSRC (Grant No. BB/N009150/1). We thank A. Das, L. Giomi, A. Maitra, M. C. Marchetti, S. Saha, and R. Selinger for many useful discussions. K.R.P. would like to thank A. M. Strydom, University of Johannesburg for hospitality.

APPENDIX A: LANGEVIN VS BROWNIAN DYNAMICS

In this appendix we show a comparison of the MSD curves for center of mass of filaments in several different regimes produced using both Langevin and Brownian dynamics simulations. Brownian dynamics simulations were performed using LAMMPS extended by a publicly available Brownian dynamics “fix” [69]. In Fig. 7 we show plots of the MSD curves for two different values of the Péclet number, Pe . From these plots it is evident that, for sufficiently long times, MSD curves obtained by those two different methods coincide in the high-activity regime and are very close to each other for low values of Pe . We attribute the discrepancy between the two in the low Pe regime to very slow collective dynamics. These results show that, at long time scales, there should be no qualitative difference between the two methods. We note, however, that Brownian dynamics simulations become unstable when the simulation time step is increased beyond 10^{-4} , which is 10 times smaller than the time step used in the Langevin dynamics simulations. This means that using Langevin dynamics simulations one can effectively reach 10 longer times compared to what is possible with Brownian dynamics simulations using the same computational resources. A detailed discussion of the numerical stability of different methods for integrating equations of motion can be found, e.g., in Ref. [60].

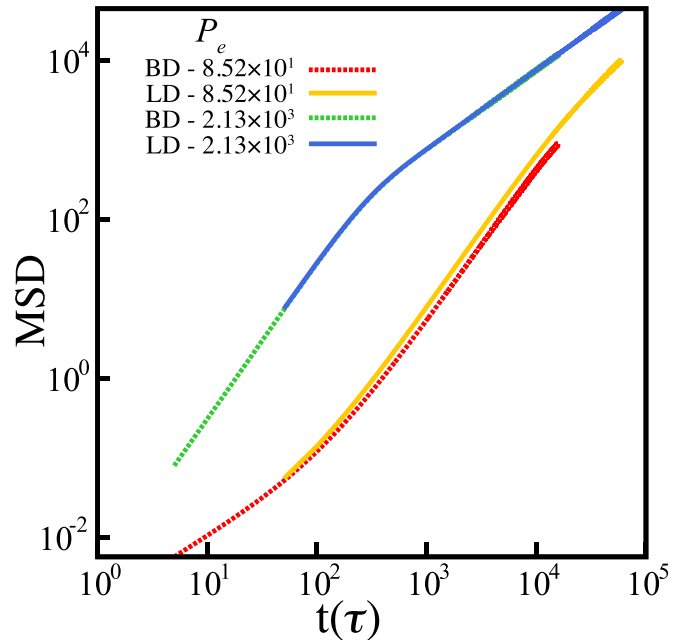


FIG. 7. Comparison of the MSD curves for two values of the Péclet number using Langevin (solid lines) and Brownian (dashed lines) dynamics simulations. For large activity, at long times, the MSD curves are indistinguishable. For smaller values of Pe , there is a small difference between the two, but we attribute it to very slow dynamics in this regime: it is likely that the steady state has not been reached during the duration of the simulation.

APPENDIX B: IDENTIFYING TOPOLOGICAL DEFECTS

In this appendix we briefly outline the method used to identify topological defects. We assign to each bead of each filament a headless (nematic) unit-length vector \mathbf{t}_i pointing along the local tangent to the contour. The direction of the

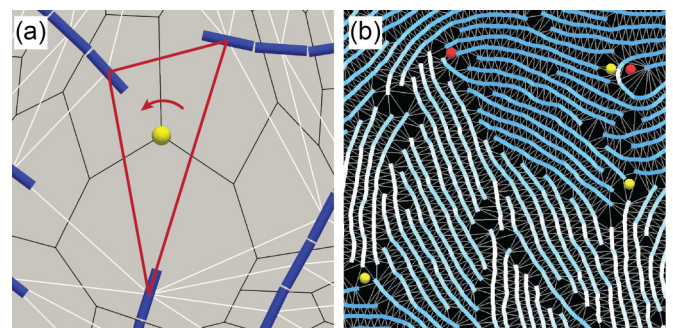


FIG. 8. Identification of topological defects. (a) Headless unit-length vectors pointing along the local tangent to the filament contour are placed at the vertices of a Delaunay triangulation (white lines). We then loop counterclockwise (red arrow) over the vertices of each triangle (marked in red) and compute a signed sum of the angles the headless vectors make with the x axis. If this sum exceeds $\pm\pi$ a defect of appropriate topological charge is placed inside that triangle. Defects (yellow ball) are located at the vertices of the Voronoi diagram (black lines) dual to the Delaunay triangulation. (b) Application of this algorithm to a snapshot of the simulation. For visualization purposes, we zoomed in on only a couple of defects.

tangent is determined as an average of the directions along the two bonds to which a bead belongs. We use the positions of the beads as vertices of a Delaunay triangulation, taking into account periodic boundary conditions. We then loop over the vertices of each triangle in the counterclockwise direction and

sum signed angles between vectors \mathbf{t}_i and the x axis. Due to the nematic symmetry these angles are between $-\pi/2$ and $\pi/2$. If the sum exceeds $\pm n\pi$ (where n is an integer), we assign a defect of charge $\pm n/2$ to the center of that triangle. This method and its application are illustrated in Fig. 8.

-
- [1] B. Alberts, A. Johnson, P. Walter, J. Lewis, M. Raff, and K. Roberts, *Molecular Biology of the Cell* (Taylor and Francis, Inc., Hamden, CT, 2008).
- [2] D. A. Fletcher and R. D. Mullins, *Nature (London)* **463**, 485 (2010).
- [3] F. Huber, J. Schnauß, S. Rönicke, P. Rauch, K. Müller, C. Fütterer, and J. Käs, *Adv. Phys.* **62**, 1 (2013).
- [4] H. M. Warrick and J. A. Spudich, *Annu. Rev. Cell Biol.* **3**, 379 (1987).
- [5] A. J. Ridley, M. A. Schwartz, K. Burridge, R. A. Firtel, M. H. Ginsberg, G. Borisy, J. T. Parsons, and A. R. Horwitz, *Science* **302**, 1704 (2003).
- [6] M. P. Sheetz and J. A. Spudich, *Nature (London)* **303**, 31 (1983).
- [7] M. P. Sheetz, R. Chasan, and J. A. Spudich, *J. Cell. Biol.* **99**, 1867 (1984).
- [8] F. Nédélec, T. Surrey, A. C. Maggs, and S. Leibler, *Nature (London)* **389**, 305 (1997).
- [9] T. Surrey, F. Nédélec, S. Leibler, and E. Karsenti, *Science* **292**, 1167 (2001).
- [10] M. S. e Silva, M. Depken, B. Stuhmann, M. Korsten, F. C. MacKintosh, and G. H. Koenderink, *Proc. Natl. Acad. Sci. U.S.A.* **108**, 9408 (2011).
- [11] D. V. Köster, K. Husain, E. Iljazi, A. Bhat, P. Bieling, R. D. Mullins, M. Rao, and S. Mayor, *Proc. Natl. Acad. Sci. U.S.A.* **113**, E1645 (2016).
- [12] I. Linsmeier, S. Banerjee, P. W. Oakes, W. Jung, T. Kim, and M. P. Murrell, *Nat. Commun.* **7**, 12615 (2016).
- [13] K. Kruse, J.-F. Joanny, F. Jülicher, J. Prost, and K. Sekimoto, *Phys. Rev. Lett.* **92**, 078101 (2004).
- [14] S. Ramaswamy, *Annu. Rev. Condens. Matter Phys.* **1**, 323 (2010).
- [15] M. Marchetti, J. Joanny, S. Ramaswamy, T. Liverpool, J. Prost, M. Rao, and R. A. Simha, *Rev. Mod. Phys.* **85**, 1143 (2013).
- [16] M. Murrell, P. W. Oakes, M. Lenz, and M. L. Gardel, *Nat. Rev. Mol. Cell Biol.* **16**, 486 (2015).
- [17] Y. Sumino, K. H. Nagai, Y. Shitaka, D. Tanaka, K. Yoshikawa, H. Chaté, and K. Oiwa, *Nature (London)* **483**, 448 (2012).
- [18] V. Schaller, C. Weber, C. Semmrich, E. Frey, and A. R. Bausch, *Nature (London)* **467**, 73 (2010).
- [19] R. G. Winkler, J. Elgeti, and G. Gompper, *J. Phys. Soc. Jpn.* **86**, 101014 (2017).
- [20] T. Sanchez, D. T. N. Chen, S. J. DeCamp, M. Heymann, and Z. Dogic, *Nature (London)* **491**, 431 (2012).
- [21] F. C. Keber, E. Loiseau, T. Sanchez, S. J. DeCamp, L. Giomi, M. J. Bowick, M. C. Marchetti, Z. Dogic, and A. R. Bausch, *Science* **345**, 1135 (2014).
- [22] S. J. DeCamp, G. S. Redner, A. Baskaran, M. F. Hagan, and Z. Dogic, *Nat. Mater.* **14**, 1110 (2015).
- [23] L. Giomi, M. J. Bowick, X. Ma, and M. C. Marchetti, *Phys. Rev. Lett.* **110**, 228101 (2013).
- [24] S. P. Thampi, R. Golestanian, and J. M. Yeomans, *Phys. Rev. Lett.* **111**, 118101 (2013).
- [25] L. Giomi, M. J. Bowick, P. Mishra, R. Sknepnek, and M. C. Marchetti, *Philos. Trans. R. Soc. London A* **372**, 20130365 (2014).
- [26] S. P. Thampi, R. Golestanian, and J. M. Yeomans, *Europhys. Lett.* **105**, 18001 (2014).
- [27] F. Alaimo, C. Köhler, and A. Voigt, *Sci. Rep.* **7**, 5211 (2017).
- [28] S. Henkes, M. C. Marchetti, and R. Sknepnek, [arXiv:1705.05166](https://arxiv.org/abs/1705.05166).
- [29] D. Kaiser, *Nat. Rev. Microbiol.* **1**, 45 (2003).
- [30] F. Peruani, J. Starruß, V. Jakovljevic, L. Søgaard-Andersen, A. Deutsch, and M. Bär, *Phys. Rev. Lett.* **108**, 098102 (2012).
- [31] F. Jülicher, K. Kruse, J. Prost, and J.-F. Joanny, *Phys. Rep.* **449**, 3 (2007).
- [32] J.-F. Joanny and J. Prost, *HFSP J.* **3**, 94 (2009).
- [33] J. Prost, F. Jülicher, and J. Joanny, *Nat. Phys.* **11**, 111 (2015).
- [34] F. Gibbons, J.-F. Chauwin, M. Despósito, and J. V. José, *Biophys. J.* **80**, 2515 (2001).
- [35] F. Nédélec, *J. Cell Biol.* **158**, 1005 (2002).
- [36] P. Kraikivski, R. Lipowsky, and J. Kierfeld, *Phys. Rev. Lett.* **96**, 258103 (2006).
- [37] T. Kim, W. Hwang, H. Lee, and R. D. Kamm, *PLoS Comput. Biol.* **5**, e1000439 (2009).
- [38] W. Jung, M. P. Murrell, and T. Kim, *Comput. Part. Mech.* **2**, 317 (2015).
- [39] K. Popov, J. Komianos, and G. A. Papoian, *PLoS Comput. Biol.* **12**, e1004877 (2016).
- [40] G. Jayaraman, S. Ramachandran, S. Ghose, A. Laskar, M. S. Bhamla, P. B. S. Kumar, and R. Adhikari, *Phys. Rev. Lett.* **109**, 158302 (2012).
- [41] H. Jiang and Z. Hou, *Soft Matter* **10**, 1012 (2014).
- [42] R. E. Isele-Holder, J. Elgeti, and G. Gompper, *Soft Matter* **11**, 7181 (2015).
- [43] A. Laskar and R. Adhikari, *Soft Matter* **11**, 9073 (2015).
- [44] A. Kaiser, S. Babel, B. ten Hagen, C. von Ferber, and H. Löwen, *J. Chem. Phys.* **142**, 124905 (2015).
- [45] A. Baskaran and M. C. Marchetti, *Phys. Rev. Lett.* **101**, 268101 (2008).
- [46] A. Peshkov, I. S. Aranson, E. Bertin, H. Chaté, and F. Ginelli, *Phys. Rev. Lett.* **109**, 268701 (2012).
- [47] T. Gao, R. Blackwell, M. A. Glaser, M. D. Betterton, and M. J. Shelley, *Phys. Rev. Lett.* **114**, 048101 (2015).
- [48] K. Sekimoto, N. Mori, K. Tawada, and Y. Y. Toyoshima, *Phys. Rev. Lett.* **75**, 172 (1995).
- [49] L. Bourdieu, T. Duke, M. B. Elowitz, D. A. Winkelmann, S. Leibler, and A. Libchaber, *Phys. Rev. Lett.* **75**, 176 (1995).
- [50] R. Chelakkot, A. Gopinath, L. Mahadevan, and M. F. Hagan, *J. R. Soc. Interface* **11**, 20130884 (2013).

- [51] T. B. Liverpool, *Phys. Rev. E* **67**, 031909 (2003).
- [52] A. Ghosh and N. S. Gov, *Biophys. J.* **107**, 1065 (2014).
- [53] T. Eisenstecken, G. Gompper, and R. G. Winkler, *Polymers* **8**, 304 (2016).
- [54] M. E. Cates and J. Tailleur, *Annu. Rev. Condens. Matter Phys.* **6**, 219 (2015).
- [55] G. S. Redner, M. F. Hagan, and A. Baskaran, *Phys. Rev. Lett.* **110**, 055701 (2013).
- [56] K. Kremer and G. S. Grest, *J. Chem. Phys.* **92**, 5057 (1990).
- [57] D. C. Rapaport, *The Art of Molecular Dynamics Simulation*, 2nd ed. (Cambridge University Press, New York, 2004).
- [58] J. D. Weeks, D. Chandler, and H. C. Andersen, *J. Chem. Phys.* **54**, 5237 (1971).
- [59] S. Plimpton, *J. Comp. Phys.* **117**, 1 (1995).
- [60] B. Leimkuhler and C. Matthews, *Molecular Dynamics: With Deterministic and Stochastic Numerical Methods* (Springer, New York, 2015).
- [61] See Supplemental Material at <http://link.aps.org/supplemental/10.1103/PhysRevE.97.022606> for movies showing behavior for several different parameter regimes.
- [62] M. Zapotocky, P. M. Goldbart, and N. Goldenfeld, *Phys. Rev. E* **51**, 1216 (1995).
- [63] X.-Q. Shi and Y.-Q. Ma, *Nat. Commun.* **4**, 3013 (2013).
- [64] M. Doi and S. F. Edwards, *The Theory of Polymer Dynamics* (Oxford University Press, Oxford, 1988), Vol. 73.
- [65] B. Reichenbach, *Ber. Dtsch. Bot. Ges.* **78**, 102 (1965); *Myxobacteriales: Schwarmenfaltung und Bildung von Protocysten* (Institut für den wissenschaftlichen Film, Göttingen, 1966).
- [66] K. Drescher, J. Dunkel, L. H. Cisneros, S. Ganguly, and R. E. Goldstein, *Proc. Natl. Acad. Sci. U.S.A.* **108**, 10940 (2011).
- [67] A. Sokolov and I. S. Aranson, *Phys. Rev. Lett.* **109**, 248109 (2012).
- [68] J. Dunkel, S. Heidenreich, K. Drescher, H. H. Wensink, M. Bär, and R. E. Goldstein, *Phys. Rev. Lett.* **110**, 228102 (2013).
- [69] G. Shi, https://github.com/anyuzx/Lammps_brownian/.